

pubs.acs.org/JPCC Article

# Distinguishing Electron and Hole Dynamics in Functionalized CdSe/CdS Core/Shell Quantum Dots Using Complementary Ultrafast Spectroscopies and Kinetic Modeling

Mohammad M. Taheri, Katherine C. Elbert, Shengsong Yang, Benjamin T. Diroll, Jungmi Park, Christopher B. Murray,\* and Jason B. Baxter\*



Cite This: J. Phys. Chem. C 2021, 125, 31-41



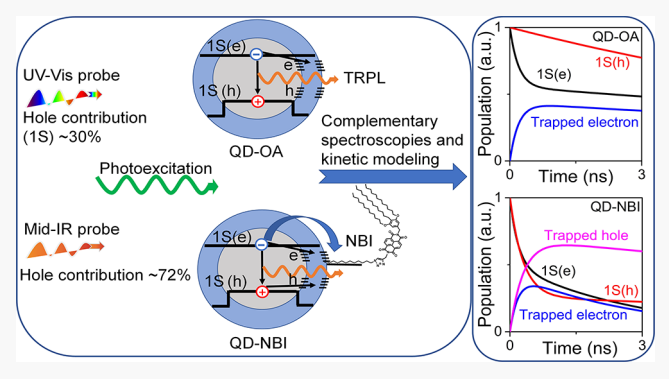
**ACCESS** 

Metrics & More

Article Recommendations

Supporting Information

ABSTRACT: The evolution of excitation energy and photogenerated charges in semiconductor quantum dots (QDs) functionalized with molecular acceptors can be probed on ultrafast time scales using techniques such as transient absorption (TA) spectroscopy. However, historical interpretations that the 1S(e)-1S<sub>3/2</sub>(h) transition in Cd-chalcogenide QDs is fully attributable to electrons may be misleading, and multiexponential models used to fit TA kinetics do not correspond directly to specific photophysical processes. Here, we present visible-wavelength and mid-IR TA and time-resolved photoluminescence measurements to inform a comprehensive kinetic model of the photoexcited CdSe/CdS core/shell QDs functionalized with passivating oleic acid (OA), hole-accepting ferrocene, or electron-accepting naphthalene



bisimide (NBI). We show that  $\sim$ 30% of the 1S signal and 72% of the IR signal can originate from holes in well-passivated core/shell QDs. We also demonstrate evidence of electron trapping in OA-capped core/shell QDs, with additional electron transfer and hole trapping in the QDs functionalized with NBI. Electron (hole) trapping and detrapping occur in 450  $\pm$  100 ps (430  $\pm$  70 ps) and 340  $\pm$  100 ps (1.1  $\pm$  0.4 ns) respectively, while the time constant for electron transfer to NBI is  $\sim$ 1.8 ns. The comprehensive picture of photophysical processes provided by the complementary ultrafast techniques and kinetic modeling can accelerate both the fundamental science and application development of nanostructured and molecular systems.

# 1. INTRODUCTION

Semiconductor quantum dots (QDs) are finding applications in optoelectronic devices such as solar cells, <sup>1,2</sup> light-emitting diodes, <sup>3,4</sup> photodetectors, <sup>5,6</sup> photocatalysts, <sup>7,8</sup> transistors, <sup>9,10</sup> and triplet photosensitizers. <sup>11,12</sup> In particular, Cd-chalcogenide QDs have been widely studied because of their excellent optical properties and their facile tunability. The energy landscape of QDs functionalized with molecular acceptors can be engineered by tuning the QD size or the chemical composition of the QD or the molecular acceptor, enabling the investigation of photophysical systems with a range of different energy levels and redox potentials for charge transfer. <sup>13,14</sup> Advancing our understanding of the electronic processes of these photophysical systems can translate into improved device performance.

Ultrafast transient absorption (TA) spectroscopy and timeresolved photoluminescence (TRPL) have advanced our knowledge of carrier dynamics in core-only and core-shell QDs, <sup>15–17</sup> QDs functionalized with accepting ligands, and donor—acceptor QD superlattices. <sup>18–26</sup> TRPL probes the photoexcited dynamics by measuring the radiative recombination of photoexcited electron—hole pairs. The origin of the TRPL signal is well understood, but ambiguities in the interpretation of TA spectra still remain after more than 20 years.

The photoinduced excited state measured by TA results from ground-state bleaching, stimulated emission, and excited-state absorption that can be monitored to reveal transient spectral information for multiple overlapping photophysical processes. Significant efforts have been made to understand electron and hole kinetics by interpreting transient spectra upon interband and intraband excitation. State-selective photoexcitation enables the preparation of well-known excitonic states that facilitate a more precise understanding of relaxation processes.

Received: July 31, 2020 Revised: December 15, 2020 Published: December 31, 2020





Generally, the 1S  $[1S(e)-1S_{3/2}(h)]$  TA bleach signal has been attributed chiefly to electrons for Cd-chalcogenide QDs for reasons that may include a higher degeneracy of populated hole states, efficient hole trapping, or both. <sup>32,36-38</sup> The contribution of holes to the band edge signal has largely been neglected. However, in 2019, Grimaldi et al. showed that while holes did not contribute to the 1S bleach in QDs with only ligand passivation, holes *did* contribute ~1/3 of the 1S signal for well-passivated CdSe/CdS/ZnS core-shell-shell QDs. <sup>39</sup> Presumably, blocking ultrafast hole trapping at the surface enabled the effect of holes to be observed in the 1S bleach.

While this recent study showed evidence for hole contribution to the 1S bleach, the importance of hole contribution to the 1S signal is still under debate. Morgan et al. in 2020 concluded that the hole contribution to the 1S bleach signal is negligible in CdSe and CdSe/CdS QDs and that the common belief regarding the dominance of electron contribution holds true. 40

In a similar vein, early studies on nanoplatelets also claimed that the band edge signal is dominated by electrons, while recent studies 41-44 demonstrated that hole contribution can be observed and strongly depends on material properties and the presence of traps. This hole contribution may have been recognized first in nanoplatelets because their shape anisotropy leads to larger splitting between light and heavy hole states, which affects the TA spectra. 45

According to these studies, an accurate interpretation of TA data requires correctly accounting for the contribution of holes. Understanding the contribution of electrons and holes to the TA signal in QDs still remains an open question, and further studies that reveal new photophysical insights would be valuable.

In addition to the ambiguity regarding the hole contribution to the 1S bleach signal, the conventional approach of fitting kinetic data with multiexponential models also inhibits understanding of the photophysics. Multiexponential models do not provide an intuitive picture of the photophysical processes, and the extracted time constants and their weights cannot directly be assigned to specific electronic processes. Additionally, the relative contributions of electrons and holes cannot be understood using the multiexponential models. The excited state inevitably undergoes complicated processes such as electron and hole trapping that compete with radiative recombination and interfacial charge transfer, which makes the interpretation of transient data almost impossible using common practices. Therefore, a systematic analysis using kinetic models based on the relevant network of photophysical processes is required to successfully distinguish and quantify the electronic processes.

Herein, we present a comprehensive picture of the electronic processes in photoexcited CdSe/CdS core/shell QDs functionalized with passivating oleic acid (OA), electron-accepting naphthalene bisimide (NBI), and hole-accepting ferrocene (Fc) ligands. We show evidence from UV—vis TA and TRPL that holes contribute to the 1S bleach by comparing the 1S kinetics for QDs functionalized with OA and Fc. We quantify the contributions of electrons and holes by comparing the 1S signal ingrowth over picosecond time scale after 1S and 2S  $\left[2S_{3/2}(h)\text{-}1S(e)\right]$  photoexcitation. Finally, we quantify the kinetics of a network of photophysical processes in QDs functionalized with OA and NBI by globally fitting a

combination of UV-vis TA, mid-IR TA, and TRPL data with a detailed kinetic model.

# 2. EXPERIMENTAL METHODS

2.1. Materials. All chemicals were used as received unless otherwise specified. Cadmium oxide (CdO, 99.99%) was purchased from Strem Chemicals, and octadecylphosphonic acid (ODPA) was purchased from PCISynthesis. Trioctylphosphine oxide (TOPO, 99%), trioctylphosphine (TOP, 90%), selenium (Se, 99.99%), sulfur (S, 99.99%), 1-octanethiol (>98.5%), octadecene (ODE, 90%), oleylamine (Olam, 70%), oleic Acid (OA, 90%), and 11-mercapto-1-undecanol (99%) were purchased from Sigma Aldrich. Oxalyl chloride (98%) and sodium borohydride (98%) were purchased from Acros Organics. Ferrocene carboxylic acid (99%) was purchased from Chem Implex Int's Inc. Sodium sulfate (anhydrous, reagent grade), silica gel (230-400 mesh, grade 60), triethyl amine (reagent grade), tetrahydrofuran, methanol, hexanes, and ethyl acetate were purchased from Fisher Scientific and used without further purification. All the solvents were ACS grade or higher. Dichloromethane was purchased from Fisher Scientific and was dried with activated molecular sieves (3A, 4 to 8 mesh, purchased from Acros Organics) before use.

Details of the synthesis of NBI and Fc ligands are provided in the Supporting Information and in the previous literature.<sup>46</sup>

2.2. Synthesis of CdSe Core and CdSe/CdS Core/Shell QDs. A modified hot-injection procedure was used to synthesize the wurtzite CdSe quantum dot cores. 47,48 First, 120 mg of CdO, 560 mg of octadecylphosphonic acid (ODPA), and 6 g of trioctylphosphine oxide (TOPO) were combined in a flask with magnetic stirring and degassed under vacuum for 1 h at 120 °C. Then, under nitrogen, the solution was heated to 340 °C until it became clear and colorless, at which point it was cooled to 150 °C and maintained under vacuum for an additional 45 min. During heating under nitrogen flow, 3.7 mL of trioctylphosphine (TOP) was injected, and once the temperature recovered 360 °C, 1 mL of TOP-Se solution (700 mg Se shots dissolved in 5 mL of TOP) was swiftly injected, and nanocrystals were allowed to grow for 20 s. After this short growing period, the heating mantle was removed, and the reaction was quenched. The nanocrystals were washed twice by precipitation using ethanol and once using isopropanol. Size-selective precipitation was used to improve the monodispersity of the cores. Finally, the sample was redispersed and stored in toluene. The resulting CdSe QDs were 3.1 nm in diameter, and the absorption peak was at 558 nm.

For the shell growth reaction, a toluene solution containing 100 nmol of CdSe QDs was loaded into a mixture of 3 mL of octadecene (ODE) and 3 mL of oleylamine. The reaction solution was degassed under vacuum at 120 °C for 1 h to completely remove toluene, water, and oxygen. After that, the reaction solution was heated to 310 °C under nitrogen flow and magnetic stirring. A calculated amount of cadmium (II) oleate and 1.2 equivalent amounts of 1-octanethiol were diluted in 6 mL of ODE separately as two solutions to be injected. During heating, when the temperature reached 240 °C, the two solutions were injected dropwise into the growth solution at a rate of 3 mL/h using a syringe pump. After 2 h of slow injection, 1 mL of OA was quickly injected into the solution to further anneal the particles at 310 °C for 10 min. The resulting CdSe/CdS core/shell QDs were precipitated by adding acetone, and then redispersed in toluene. Size-selective

precipitation by precipitation-redispersion was used to improve the monodispersity, and the particles were redispersed in toluene. The high-resolution transmission electron microscopy (HRTEM) and wide-angle electron diffraction images of the core/shell QDs are shown in Figure S1.

- 2.3. Ligand-Exchange Procedure. A solution of 18 mg of ligand dissolved in chloroform was mixed with a 10 mL solution of 1.8 mg/mL OA-capped CdS/CdSe core-shell QDs in hexanes and stirred at 50 °C overnight. The reaction was cooled to room temperature, and ethanol was added until precipitation was observed. The resulting precipitate was collected by centrifugation (8000 rpm, 3 min), and the supernatant liquid was discarded. The solid was redispersed in hexane and precipitated by the addition of ethanol. This step was repeated at least twice to remove any excess ligand before the QDs were finally dispersed in chloroform.
- 2.4. Analytical Techniques. 2.4.1. NMR. <sup>1</sup>H NMR (500 MHz) and <sup>13</sup>C NMR (126 MHz) spectra were recorded on Bruker UNI500.  $^{1}$ H and  $^{13}$ C chemical shifts ( $\delta$ ) are reported in ppm while coupling constants (J) are reported in Hertz (Hz). The multiplicity of signals in <sup>1</sup>H NMR spectra is described as "s" (singlet), "d" (doublet), "t" (triplet), "q" (quartet), "p" (pentet), "dd" (doublet of doublets), and "m" (multiplet). All spectra were referenced using solvent residual signals (CDCl3:  $^{1}\text{H}$ ,  $\delta$  7.27 ppm;  $^{13}\text{C}$ ,  $\delta$  77.2 ppm).
- 2.4.2. Mass Spectroscopy. Accurate mass measurement analyses were conducted on an LCT Premier XE, time-offlight, liquid chromatography-mass spectroscopy (LCMS) with electrospray ionization (ESI). Samples were taken up in a suitable solvent for analysis. The signals were mass-measured against an internal lock mass reference of leucine enkephalin for ESI-LCMS. Waters software calibrated the instruments and reported the measurements using neutral atomic masses. The mass of the electron is not included.
- 2.4.3. Electron Microscopy. TEM micrographs were collected using a JEOL 1400 microscope operated at 120 kV. HRTEM micrographs and electron diffraction were collected using a JEOL F200 microscope operated at 200 kV. The transmission electron microscope was calibrated using a MAG\*I\*CAL TEM calibration standard.
- 2.5. UV-vis TA. We conducted femtosecond UV-vis TA measurements using the output of a regeneratively amplified Ti:sapphire laser (Coherent Libra, 50 fs, 1 kHz, 3.5 W) that was split to generate the pump and probe beams, which were then sent to an Ultrafast Systems Helios spectrometer. The pump wavelength was selected using an optical parametric amplifier. A broad-band white-light continuum (WLC) probe from 340-700 nm was generated by focusing an 800 nm pulse into a CaF2 crystal window. We recorded the transient absorption data as  $\Delta A = -\log \left(\frac{I_{\mathrm{ex,T}}}{I_0,T}\right)$ , where  $I_{\mathrm{ex,T}}$  is the intensity of the transmitted probe of the excited sample and  $I_{0,T}$  is the intensity of the transmitted probe without photoexcitation. QDs were suspended in chloroform in a 2mm quartz cuvette. Photoexcitation was with either 1S ( $\sim$ 600 nm) or 2S (~550 nm) photon energy. The instrument response function is 130-140 fs, as determined by both pure solvent response and the deconvolution of the signal rise for
- 2.6. Mid-IR TA. Mid-IR TA was measured with the QD samples in deuterated chloroform in a 1-mm CaF<sub>2</sub> IR cell. The QD samples were photoexcited with a 2S (~550 nm, ~35 fs) pump and the probe pulses of 7–10  $\mu$ m. The pump and probe

pulses were generated from the output of a 2 kHz 30 fs Ti:sapphire laser (SpectraPhysics) using separate optical parametric amplifiers. The pump beam was mechanically chopped at 1 kHz to enable pump on and pump off signals. The 2 kHz probe beam was directed through the sample into a spectrometer on to a mercury cadmium telluride array detector.

**2.7. TRPL.** TRPL spectroscopy was performed using a highspeed streak camera (Hamamatsu). The QD solutions in deuterated chloroform were contained in a 1-mm CaF<sub>2</sub> IR cell. The QD samples were photoexcited with a 2S (~550 nm, ~35 fs) pump ( $\langle N \rangle \sim 0.2$ ) and measured with  $\sim 10$  ps time resolution. The PL kinetics up to 700 ps at the 1S energy (~600 nm) state were collected for the kinetic analysis.

We used a high-speed streak camera with a short instrument response function (IRF) ( $\sim 10$  ps) and range up to 700 ps in this work to capture the fast TRPL kinetics in sub-ns time scale. We also performed TRPL with an IRF of ~620 ps and a range up to ~100 ns as a reference because that is more conventionally used in the field to determine the quality of the samples.

All TA and TRPL measurements were performed under low enough fluence so that kinetics were independent of fluence. To confirm that Auger recombination and charged QDs have a negligible impact on kinetics, TA experiments were performed under different pump fluences (corresponding to  $\langle N \rangle \sim 0.04$ to 0.29), with and without rapidly stirring the solution. The samples were stirred using a magnetic stirring bar and a rotary magnet (close to the cuvette) to stir the solution around an axis pointing in the small dimension of the cuvette. The normalized kinetics are similar under all these conditions, as shown in Figure S2. Therefore, the impact of higher-order recombination and charging can be excluded from our kinetic analysis. Calculations for <*N*> are described in the Supporting Information, Figure S3.

# 3. RESULTS AND DISCUSSION

All experiments used CdSe/CdS core-shell QDs with 3.1 nm core diameter and 1.7 nm thick shell unless otherwise noted. Nanosecond TRPL of these QDs capped with OA showed a slow component of ~21 ns that is often associated with radiative lifetime; and the PL quantum yield was ~64%, as shown in Figures S4-5. These metrics are typical of highquality CdSe QDs of this size. 40 Figure 1 shows the UV-vis absorption of the CdSe/CdS core-shell QDs capped with OA and NBI (QD-OA, QD-NBI), along with a schematic of the optical transitions. For these studies, about 30% of native OA was exchanged with NBI during the ligand-exchange process, as our previous studies suggest that optimal electron transfer occurs with a mixed ligand shell for this system<sup>46</sup> because of how the ligands interact. Two distinct peaks from NBI can be seen in the inset of the UV region for the QD-NBI case. The distinct visible absorption features indicate highly monodisperse QDs and allow state-specific photoexcitation. These features are linked to optical transitions as guidance for designing and interpreting TA experiments. 1S excitation generates electrons and holes directly at the band edge energy levels (1S(e) and 1S<sub>3/2</sub>(h)), while 2S excitation generates hot holes,  $2S_{3/2}(h)$ , along with the band edge electrons.

3.1. Evidence of Hole Contribution to the TA Signal. The common consensus regarding the interpretation of TA data for Cd-chalcogenide QDs has been that the hole contribution to the TA signal is negligible and can be

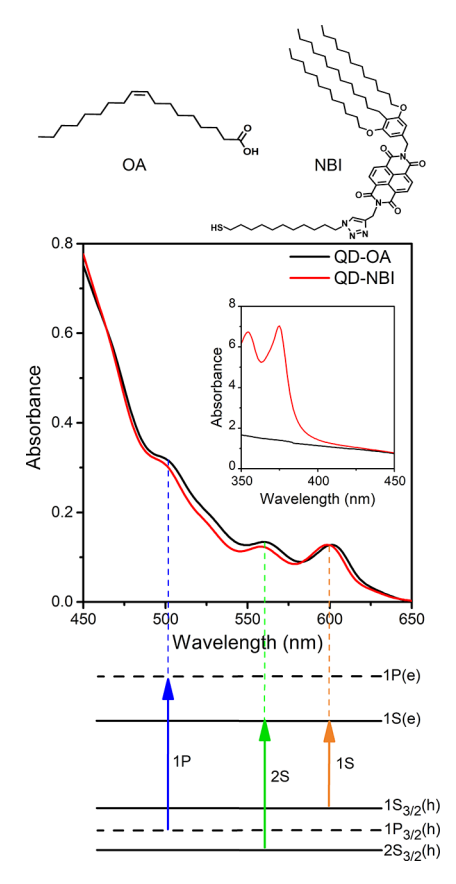


**Figure 1.** UV—vis absorption spectra for QDs with OA and NBI, with absorption features mapped to corresponding optically allowed transitions. Inset shows UV absorption, with distinct absorption features from the NBI moieties.

excluded. A recent study showed that the contribution of holes to the 1S TA bleach may be zero when hole trapping is fast but is  $\sim 1/3$  for QDs that are well-passivated with a double shell. Here, we provide additional evidence for the contribution of holes by first assessing the growth of the 1S TA bleach upon the selective photoexcitation of the 1S and 2S states and then analyzing the changes in kinetics in the presence of the hole-accepting Fc ligand.

Following the approach presented by Grimaldi et al., 39 we performed a series of UV-vis TA experiments on QD-OA (Figure 2a) to quantify the electron and hole contribution to the TA signal by probing the 1S transition. When photoexciting the QDs with the 1S pump, a prompt signal rise within the instrument response time was observed for the 1S bleach as both the electrons and holes directly populate the band edge states. However, a slower increase of the 1S bleach was observed when the QDs were selectively photoexcited with 2S photons. The electrons occupy the same band edge state as that under 1S resonant excitation, but the hot holes generated with 2S photons do not contribute to the 1S bleach until they cool to the band edge; hence, the difference in kinetics indicates the time scale for hole cooling and provides a measure of the contribution of holes to the TA bleach signal. A schematic of these processes is depicted in Figure 2b.

The magnitude of the TA signal is proportional to the sum of electron and hole contributions and can be defined as TA(t) = (1 - x)E(t) + xH(t). E(t) and H(t) represent the electron and hole kinetics, and x is the fractional hole contribution. An exponential increase convoluted with the IRF was applied to

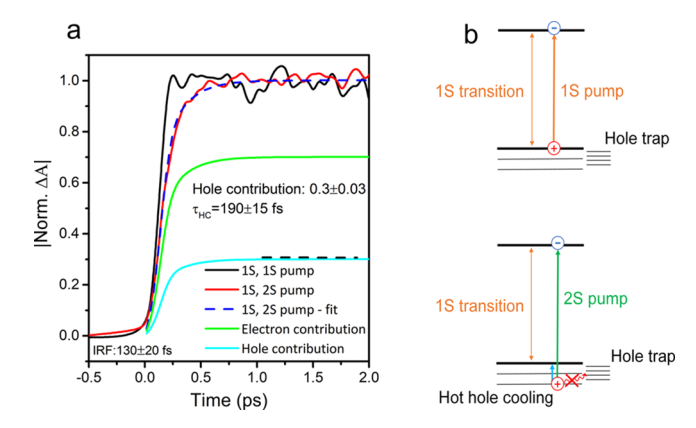
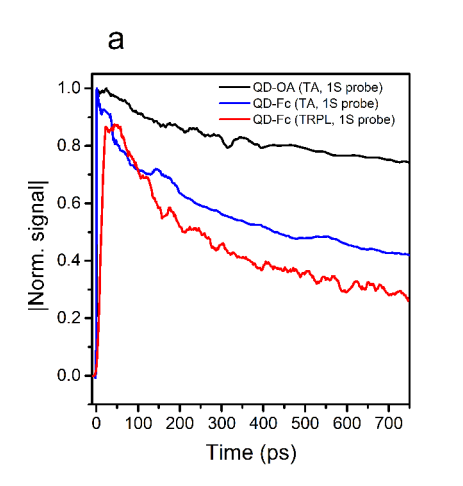


Figure 2. Quantifying the hole contribution to the 1S signal. (a) 1S TA bleach kinetic with selective 1S and 2S pump. (b) Schematic of 1S pump excitation vs 2S pump excitation. To effectively detect hole contribution from the TA signal, the hot hole-cooling process has to be slower than the hot hole-trapping process and the IRF.

the kinetics to quantify the electron and hole contribution to the TA signal. Further details on the procedure and equations for extracting the hole contribution, following reference 39, are available in the Supporting Information. The hole contribution was estimated to be  $\sim\!30\%$  of the overall 1S transition magnitude, with a hot hole-cooling time of 190 fs.

Previous literature on CdSe QDs without shells did not report any difference in the signal ingrowth when the 1S bleach signal was monitored for 1S vs 2S excitation. 38,49 That result is consistent with our own observations of CdSe-OA (Figure S6). Both in our work here and in that of Grimaldi et al., 39 the difference in the signal ingrowth only occurs in the presence of thick or multilayered shells. Grimaldi et al. proposed that ultrafast hole trapping in the core-only structure prevents hole cooling to the band edge so that the signal growth predominantly arises from the electron population at the band edge. In contrast, thick or multilayer shells can more completely passivate hole traps such that hole cooling to the band edge is observed. An alternative explanation could be that the hole-cooling process in core-only structures could be faster than the IRF, such that the hole-cooling process and its effect on the 1S signal growth cannot be detected. Faster hole cooling in core-only compared to core-shell QDs has been observed, but the evidence of hole contribution to the 1S bleach was not observed even with 40 fs IRF.<sup>3</sup>

The influence of holes on the 1S TA kinetics was also observed using the hole-accepting Fc ligands grafted onto 2.6 nm core with 1.7 nm shell CdSe/CdS QDs. A single batch of high-quality QDs was not enough for full characterization with multiple ligands, and the QDs synthesized for this study were slightly smaller than the others. Fc is expected to accept holes on its oxidation potential, which is 0.8–1 eV above the CdSe valence band. The decay of the 1S bleach for QD-Fc is faster than that for QD-OA, Figure 3a. The routes for signal quenching for QD-OA include electron and hole trapping as well as radiative recombination, while in QD-Fc, holes can additionally transfer from QDs into Fc. The possibility of electron transfer from QDs into Fc is ruled out because the lowest unoccupied molecular orbital (LUMO) energy level of Fc is above the conduction band edge of the QDs. Therefore, the faster kinetics for the hybrid structure is likely due to the quenching of holes by Fc, although we cannot



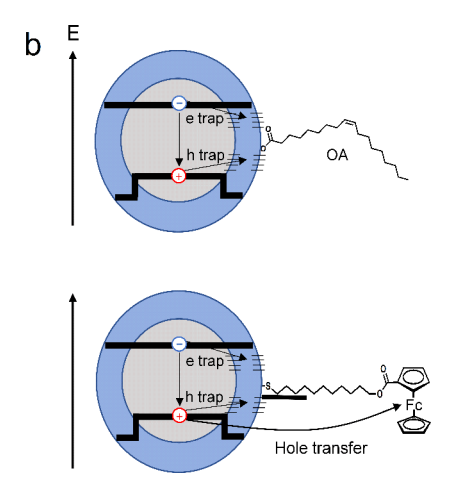


Figure 3. (a) TA 1S probe kinetics for QD-OA and QD-Fc, along with TRPL kinetics of QD-Fc. (b) Schematic of the quenching mechanisms in QD-OA and QD-Fc.

rule out the trapping of carriers at the defects on the CdS surface introduced during ligand exchange. 52

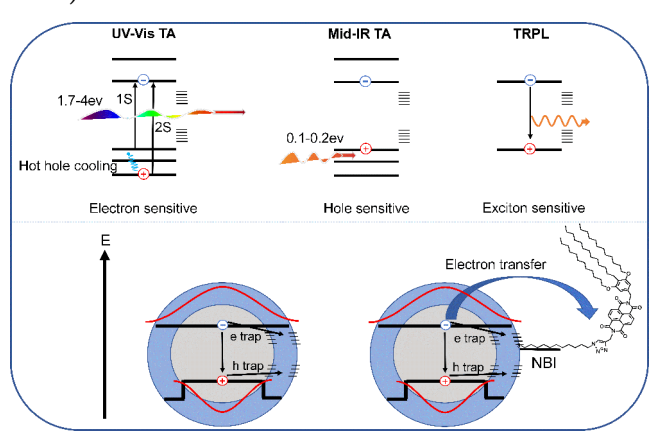
Figure 3b schematically illustrates different quenching mechanisms for these structures. When fit with a biexponential function, the amplitude-weighted average lifetime for QD-OA is ~8.7 ns and that for QD-Fc is ~1.6 ns with TA and ~800 ps with TRPL, which is comparable to the previously reported values. <sup>53,54</sup> The details of the exponential fit are available in the Supporting Information, Figure S7 and Table S1. This experiment indicates that holes affect the TA signal, so the contribution of holes should be considered when analyzing the TA data. Time-resolved spectral data for QD-OA and QD-Fc are shown in Figure S8A,B.

The PL decay for QD-Fc is faster than the 1S TA decay. PL requires both an electrons and a hole in the QD, and the absence of either the electron or the hole would eliminate radiative recombination. On the other hand, the 1S TA signal is independently sensitive to both the electron and hole contributions, and the extraction of either of the carriers would result in a partial quenching of the TA signal. Comparing the PL and TA decays further highlights the fact that the TA signal is additive and originates from both electrons and holes. Thus, a fully accurate interpretation of the TA data needs a thorough understanding of the electronic contribution. In the following sections, we further demonstrate the importance of the hole contribution to accurately interpret transient data.

3.2. Comprehensive Picture of Electronic Processes from UV-vis TA, Mid-IR TA, and TRPL. Combining UV-vis TA with mid-IR TA and TRPL can provide a more comprehensive picture of electronic processes. This picture is developed by comparing the photoexcited kinetics with different spectral probe energies. The upper panel of Scheme 1 illustrates the transitions probed using each technique in this study. As mentioned earlier, UV-vis TA probes interband transitions (1.7–4 eV) that are mostly electron-sensitive; we showed that ~70% of the 1S transition magnitude originated from electrons. UV-vis TA spectra are shown in Figure S9A,B. PL kinetics are sensitive to the product of electron and hole population; therefore, TRPL probes the carrier with the fastest relaxation time (either electrons or holes).

Our mid-IR TA measurements exhibited probe energies of 0.12–0.17 eV corresponding to intraband transitions. Mid-IR TA spectra for QDs with OA and NBI are shown in Figure S9C,D. The  $2S_{3/2}(h)$ - $1S_{3/2}(h)$  transition energy of  $\sim$ 0.15 eV

Scheme 1. Illustration of Transitions Probed Using Each Technique (Upper Panel) and Schematic Routes for Carrier Quenching Mechanisms in QD-OA and QD-NBI (Lower Panel)<sup>a</sup>



"The CdSe/CdS core/shell forms a quasi-type II structure because of the small conduction band offset. 58,59 The black lines show the conduction and valence band energy alignment in the CdSe/CdS structure. The red lines indicate the electronic wavefunctions (delocalized electrons in the conduction bands and holes localized in the CdSe core).

for holes is similar to the probe energy chosen for mid-IR TA experiments, whereas the 1P(e)-1S(e) transition energy of  $\sim 0.3$  eV for electrons is significantly larger. <sup>56</sup> Based on the probe energy chosen for the mid-IR TA measurements, we assign the time evolution data in the mid-IR measurements to be mostly hole-sensitive. <sup>37,57</sup> We quantify this assignment in Section 3.3 using global kinetic modeling.

Figure 4a shows that the 1S decay for QD-NBI is faster than that for QD-OA. As illustrated in Scheme 1, there could be multiple routes for the quenching of the 1S bleach for QD-OA and QD-NBI. The routes for signal loss for QD-OA are radiative recombination and electron and hole trapping at the core/shell interface or shell surface. The faster kinetics in QD-NBI could originate from the additional pathways of electron transfer from QDs into NBI and additional trapping due to changes in the surface sites on the shell. These processes cannot be distinguished by employing only UV-vis TA; however, we will show that the complementary information

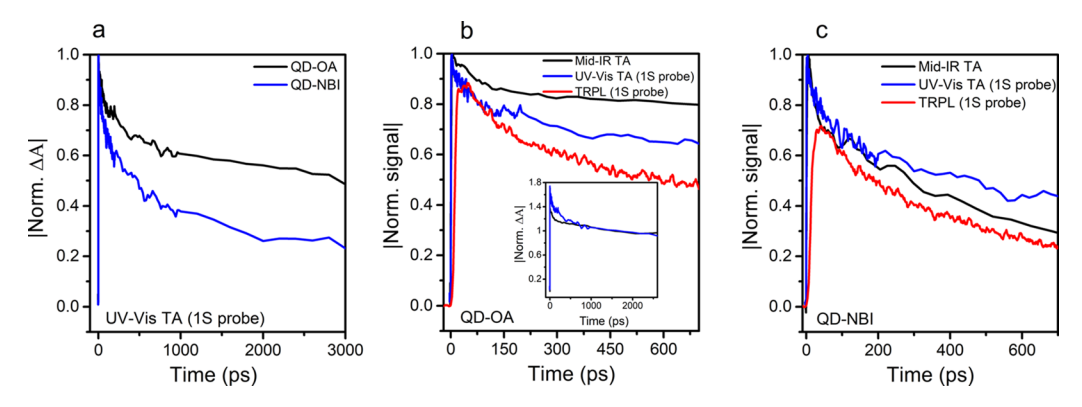


Figure 4. Comparing UV—vis TA, mid-IR TA, and PL kinetics for QDs with OA and NBI. (a) UV—vis TA kinetics with 1S probe for QD-OA and QD-NBI. UV—vis, mid-IR, and PL kinetics for (b) QD-OA, and (c) QD- NBI. All experiments were conducted with a 2S pump and low enough power to minimize the effect of higher-order recombination on kinetics. All the TA and TRPL data sets were smoothed using adjacent-averaging (10-point window) with a parabolic weight function for better visualization and comparison of the data. The inset in Figure 4b shows normalized kinetics with respect to longer time scale for the QDs with 1S and mid-IR probe.

provided by mid-IR TA and TRPL can allow the differentiation of these processes.

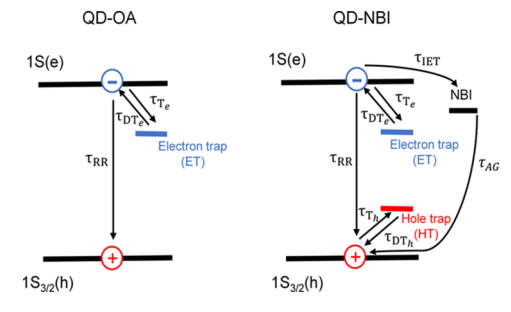
Figure 4b shows the comparison of the kinetics from UVvis TA (1S probe), mid-IR TA, and PL for QD-OA. A representative averaged kinetic for the mid-IR TA has been chosen for this study because the normalized kinetics are similar over a range of wavelengths, Figure S10A,B. Kinetics are faster for the 1S probe than that for the mid-IR probe over the first few 100 ps. Because the 1S probe is electron-sensitive and the mid-IR probe is hole-sensitive, this difference in kinetics indicates that electrons are trapped faster than holes. Electrons could trap at unpassivated defect sites (dangling bonds, defects or Se, S lone pairs)<sup>30,60-63</sup> at the core/shell interface or at the CdS shell defect sites because electrons are delocalized over the core/shell structure (Scheme 1). The 1S and mid-IR probe kinetics are closely matched on the nanosecond time scale (inset in Figure 4b). The removal of electrons and holes on similar time scales may indicate band edge recombination. The PL kinetics are slightly faster than the TA kinetics (1S probe) because TA probes the sum of electrons and holes while PL requires both the carriers to be present.

We also measured kinetics with each technique for the QDs with NBI, Figure 4c. All the three techniques show faster kinetics with NBI than with OA. While interfacial electron transfer is expected to lead to a faster decay of the 1S and PL probes, the faster mid-IR kinetic would not result from only electron transfer because the mid-IR probe is primarily holesensitive. Interestingly, the mid-IR TA kinetic is even slightly faster than the 1S probe. Therefore, we conclude that ligand exchange may induce more hole traps in addition to enabling the electron transfer from QDs into NBI. It may also induce additional electron trapping compared to QD-OA. The traps induced by ligand exchange would be on the surface of CdS, although hole trapping would require tunneling through the CdS shell because the holes are localized in the CdSe core (Scheme 1). PL has a comparable kinetics as that of the mid-IR, which further reveals that the photoexcited PL kinetics is influenced by the carrier with the fastest relaxation time, which in this case is holes. Further studies are required to fully understand the origin of electron and hole trapping and its dependence on the structural and chemical properties of the QDs.

The TA data sets presented in Figure 4 were normalized with respect to their absolute peak values that occur within sub-ps to ps time scale. However, because of slower instrument response for the TRPL measurements (with the IRF of  $\sim 10$  ps vs 130 fs for TA), the measured PL peak appeared to be around 40 ps (see Figure S11 for the raw TRPL data sets). To avoid any misinterpretation in the kinetic analysis, we have matched the normalized TRPL data sets to the fastest TA kinetic at  $\sim 40$  ps. Our kinetic model described below is not affected by this artifact of visualization.

**3.3. Global Kinetic Modeling.** By conducting a series of ultrafast measurements with unique spectral probe energies, we were able to identify the underlying electronic processes such as electron and hole trapping within the structures. In this section, we propose a first-order kinetic model to further analyze and quantify the electronic processes. Scheme 2 illustrates the proposed kinetic model for QD-OA and QD-NBI

Scheme 2. Schematic of the Processes Involved in the Global Kinetic Model for the QDs with OA and NBI<sup>a</sup>

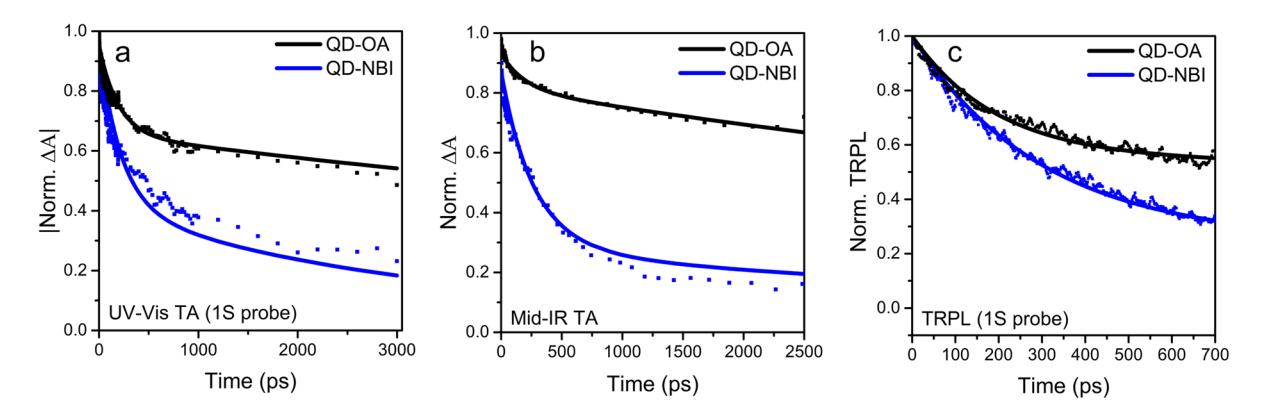


"Electron trapping and detrapping time constants ( $\tau_{\rm T_e}$ ,  $\tau_{\rm DT_e}$ ) and the radiative recombination time constant ( $\tau_{\rm RR}$ ) are shared in both the structures

We used the following equations to represent the kinetics of electrons mapped to processes shown in Scheme 2 for the trapping/detrapping of electrons and radiative recombination in QD-OA:

$$\frac{\mathrm{d}S_{\mathrm{e}}}{\mathrm{d}t} = -\frac{S_{\mathrm{e}}}{\tau_{\mathrm{RR}}} - \frac{S_{\mathrm{e}}}{\tau_{\mathrm{T_{e}}}} + \frac{\mathrm{ET}}{\tau_{\mathrm{DT_{e}}}} \tag{1}$$

## Including both electron and hole contributions fits all data



# Cannot fit all data when excluding hole contributions

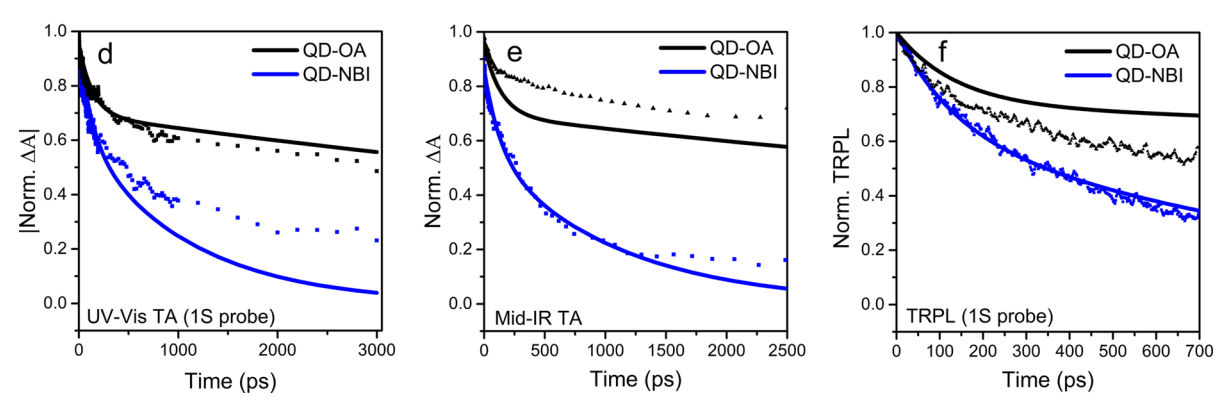


Figure 5. Experimental (dots) and modeled (solid lines) kinetics for QD-OA and QD-NBI for (a) UV-vis TA, (b) mid-IR TA, and (c) PL data sets. Also, the fitting results when excluding the contribution of holes from the model are presented for (d) UV-vis TA, (e) mid-IR TA, and (f) PL data sets

$$\frac{\mathrm{dET}}{\mathrm{d}t} = \frac{S_{\mathrm{e}}}{\tau_{\mathrm{T_{e}}}} - \frac{\mathrm{ET}}{\tau_{\mathrm{DT_{e}}}} \tag{2}$$

Here,  $S_{\rm e}$  represents the population of the 1S(e) energy state, and ET represents the population of the electron trap state. Also,  $\tau_{\rm RR}$  is the radiative recombination time constant,  $\tau_{\rm T_e}$  is the electron trapping time constant, and  $\tau_{\rm DT_e}$  is the electron-detrapping time constant from the trap state to the 1S(e) energy state. The selection of only electron trapping is based on our observation shown in Figure 4b that the 1S bleach that receives  $\sim 2/3$  of its influence from electrons decays significantly faster than the mid-IR probe that is sensitive to holes.

For QD-NBI, we used the following set of equations that allow for interfacial electron transfer to the acceptor and hole trapping/detrapping in addition to electron trapping/detrapping and radiative recombination as in QD-OA:

$$\frac{\mathrm{d}S_{\mathrm{e}}}{\mathrm{d}t} = -\frac{S_{\mathrm{e}}}{\tau_{\mathrm{RR}}} - \frac{S_{\mathrm{e}}}{\tau_{\mathrm{T_{e}}}} - \frac{S_{\mathrm{e}}}{\tau_{\mathrm{IET}}} + \frac{\mathrm{ET}}{\tau_{\mathrm{DT_{e}}}} \tag{3}$$

$$\frac{\mathrm{dNBI}}{\mathrm{d}t} = \frac{S_{\mathrm{e}}}{\tau_{\mathrm{IET}}} - \frac{\mathrm{NBI}}{\tau_{\mathrm{AG}}} \tag{4}$$

$$\frac{\mathrm{dET}}{\mathrm{d}t} = \frac{S_{\mathrm{e}}}{\tau_{\mathrm{T}_{\mathrm{e}}}} - \frac{\mathrm{ET}}{\tau_{\mathrm{DT}_{\mathrm{e}}}} \tag{5}$$

$$\frac{dS_{h}}{dt} = -\frac{S_{h}}{\tau_{RR}} - \frac{S_{h}}{\tau_{T_{h}}} + \frac{HT}{\tau_{DT_{h}}} - \frac{S_{h}}{\tau_{AG}}$$
(6)

$$\frac{\mathrm{dHT}}{\mathrm{d}t} = \frac{S_{\mathrm{h}}}{\tau_{\mathrm{T_{h}}}} - \frac{\mathrm{HT}}{\tau_{\mathrm{DT_{h}}}} \tag{7}$$

Here, NBI represents the population of the acceptor state,  $S_{\rm h}$  represents the  $1S_{3/2}(h)$  energy state, and HT represents the hole-trap state. Also,  $\tau_{\rm IET}$  is the interfacial electron transfer time constant from QDs into NBI,  $\tau_{\rm AG}$  is the electron-recovery time constant from the acceptor to the ground state,  $\tau_{\rm T_h}$  is the hole-trapping time constant, and  $\tau_{\rm DT_h}$  is the hole-detrapping time constant from the trap state to the  $1S_{3/2}(h)$  state. Hole trapping/detrapping was included for QD-NBI based on the slightly faster kinetics of the mid-IR probe compared to the 1S probe, as shown in Figure 4c. The radiative recombination time constant and the electron trapping and detrapping time constants are shared for both QD-OA and QD-NBI.

Global fitting using eqs 1-7 was applied to the collective set of UV-vis TA (1S probe), mid-IR TA, and TRPL data in Figure 4. The hole contribution to the 1S TA signal was set as  $\sim 0.3$ , as determined in Section 3.1. For the mid-IR data sets, hole contribution was set as a fitting parameter because it is not known. The time constants illustrated in Scheme 2 were obtained by minimizing the error between the numerical solution to eqs 1-7 and the experimental data sets using the

Table 1. Parameters for the Best Global Fit to the Experimental UV-vis TA, Mid-IR TA, and TRPL Data Sets, with R<sup>2</sup> = 0.90<sup>a</sup>

electron trap $( au_{\mathrm{T_e}})$	electron detrap $( au_{ ext{DT}_e})$	hole trap $( au_{ extsf{T}_{ extsf{h}}})$	hole detrap $( au_{ ext{DT}_{ ext{h}}})$	radiative recombination $( au_{RR})$	acceptor to ground state $( au_{ ext{AG}})$	interfacial electron transfer $( au_{ ext{IET}})$	fractional hole contribution in mid-IR
450 ± 100 ps	$340 \pm 100 \text{ ps}$	$430 \pm 70 \text{ ps}$	$1.1 \pm 0.4 \text{ ns}$	> > 3 ns	> > 3 ns	$1.8 \pm 0.8 \text{ ns}$	$0.72 \pm 0.05$

<sup>a</sup>The time constants for radiative recombination ( $\tau_{RR}$ ) and the acceptor to ground state ( $\tau_{AG}$ ) are beyond 3 ns, which is the range of our TA instrument.

genetic algorithm built-in optimization function in MATLAB. Normalized kinetics instead of actual carrier concentrations were used in the model because measuring carrier concentration is not straightforward. Because the kinetic model was developed assuming first-order processes, the absolute magnitude of concentrations in the model does not affect the extracted time constants.

The normalized experimental and modeled kinetics for the best-fit scenario are shown in Figure 5a—c. All six kinetic traces comprising the three ultrafast measurements of QD-OA and QD-NBI can be fit well with one set of six model parameters (not counting the two parameters with time constants much larger than our experimental time range), with  $R^2=0.9$ . The time constants from the best-fit numerical solution are summarized in Table 1. For the best-fit scenario, six fitting parameters, each with a direct physical interpretation based on the experimental observations, were included in the kinetic model (Scheme 2). The uncertainties reported in Table 1 indicate the range over which that parameter can be set while maintaining  $R^2>0.85$  and letting the other parameters vary.

Our kinetic model offers a more precise way to quantify the time scale of all the photophysical processes that affect the time-resolved data, including the competition between the interfacial electron transfer and electron and hole trapping. The normalized population of the electrons and holes at the band edge and trap states are presented in Figure S12 using the best-fit parameters in Table 1. The electron trapping and detrapping in this study occur on  $450 \pm 100$  and  $340 \pm 100$  ps time scales, respectively, while hole trapping and detrapping occur in 430  $\pm$  70 ps and 1.1  $\pm$  0.4 ns, respectively. The reported values for charge trapping for Cd-chalcogenide QDs range from picoseconds to microseconds and strongly depend on the degree of passivation at the core/shell interface, the number of unbound sites at the shell surface, and the chemical and structural nature of the QDs. 34,53,64-68 The rate of interfacial electron transfer depends on the electronic and molecular structure of the acceptor, the number of acceptors per QD, and the interactions between the NBI moieties.<sup>44</sup> Interfacial electron transfer occurred on the nanosecond time scale (1.8  $\pm$  0.8 ns) for our system. While electron transfer contributes some to the overall signal loss in the QD-NBI structure, charge trapping in this study occurs faster than electron transfer. As shown in Figure 4b,c and based on our analysis, electron and hole trapping significantly contribute to the overall signal loss in the QDs. This conclusion highlights the importance of the comprehensive understanding of the electronic processes; a naive interpretation of QD-OA and QD-NBI kinetics may lead to an erroneous conclusion that the differences are entirely due to interfacial electron transfer.

This model also highlights the importance of quantifying electron and hole contribution to TA probes of different energies. The best-fit value of the fractional hole contribution for mid-IR was  $\sim$ 0.72, which is consistent with our result discussed in Section 3.2 that the mid-IR range is hole-sensitive. If the hole contribution is excluded for all the data sets, the

model cannot fit the experimental data. Figure 5d—f shows a significant deviation of this revised model from all the data sets, even with all other parameters adjustable. Extracted constants from the fit are available in Table S2. This model further highlights the importance of hole contribution for accurate kinetic analysis.

We also performed a series of other sensitivity analyses to test the importance of the parameters in the model. The details of other sensitivity analyses, such as the exclusion of electron or hole trapping or detrapping processes, are available in Figures S13–S17 and Table S2. Other models with different processes excluded show significantly worse fit, indicating that the array of parameters selected in our model is appropriate.

The conventional alternative to our global kinetic model is a set of multiexponential functions, a few examples of which are presented in references. 15,18,19,69-71 In that case, TA kinetics

can be fit as 
$$1S_{\text{QD-OA}} = \sum_{i=1}^{n} a_i \exp\left(-\frac{t}{\tau_{\text{QD-OA}_i}}\right)$$
 and

$$1S_{\text{QD-NBI}} = \sum_{i=1}^{n} A_i \exp\left(-\frac{t}{\tau_{\text{QD-NBI}_i}}\right), \text{ where the bleach signals}$$

are normalized to their maximum absolute value. To accurately fit the kinetics using a multiexponential function, eight fitting parameters are required. The details of the fitting results are provided in Tables S3-S7 and Figures S18-20. The main problem with such an approach is that the extracted values from a multiexponential function do not have any physical meaning and cannot be directly assigned to a specific electronic process. For instance, the relative electron and hole contributions cannot be determined or understood. Additionally, the global kinetic model essentially requires only six fitting parameters to adequately fit the UV-vis TA, mid-IR TA, and TRPL data sets (because  $\tau_{RR} \& \tau_{AG} \gg 3$ ns, the fit quality is insensitive to these time constants), while the multiexponential function requires eight fitting parameters to fit just the UV-Vis TA kinetics. Considering these facts, the global kinetic model is a much more powerful approach to understand the contribution of electronic processes to the transient data as compared to conventional multiexponential fitting models.

# 4. CONCLUSIONS

Precise interpretation of TA data requires a comprehensive understanding of relative electron and hole contributions and competition between electronic processes such as charge transfer to a molecular acceptor, carrier trapping, and recombination. While the consensus in the field has been to exclude the hole contribution from the TA analysis, we have demonstrated through experiments and modeling that holes affect the TA results for CdSe QDs with thick CdS shells and can contribute  $\sim\!30\%$  to the 1S transition and  $\sim\!72\%$  to the mid-IR probe range. Researchers usually conduct only UV—vis TA measurements for Cd-chalcogenide QDs to understand the electronic processes, but uncovering all the ultrafast mechanisms might be challenging or impossible. In this work, we

have demonstrated the benefit of employing multiple complementary ultrafast tools to better understand electronic processes. By comparing the 1S probe (UV-vis TA) to mid-IR TA kinetics, we have shown evidence of electron trapping for the QDs with OA and additional electron transfer and hole trapping for QDs with NBI. We have also presented a detailed global kinetic model to describe the UV-vis TA, mid-IR TA, and TRPL data sets. The kinetic modeling approach presented herein can provide more comprehensive and specific insights into electronic processes, with fitting parameters that correspond directly to electronic processes. Our kinetic model also has fewer fitting parameters than conventional multiexponential fits. The photophysical insights gained from a combination of multiple ultrafast techniques and systematic modeling can be applied to improve the understanding of a wide array of QD-based materials and heterostructures.

# ASSOCIATED CONTENT

# **5** Supporting Information

The Supporting Information is available free of charge at https://pubs.acs.org/doi/10.1021/acs.jpcc.0c07037.

Further details regarding the synthetic details, experimental procedures, HRTEM image of the QDs, more details regarding the calculations of hole contribution, spectroscopic data of the QDs, calculation of average excitons per QD, sensitivity analysis for the kinetic model, and exponential fitting (PDF).

# AUTHOR INFORMATION

## **Corresponding Authors**

Christopher B. Murray — Department of Chemistry, University of Pennsylvania, Philadelphia, Pennsylvania 19104, United States; Department of Materials Science and Engineering, University of Pennsylvania, Philadelphia, Pennsylvania 19104, United States; Email: cbmurray@sas.upenn.edu

Jason B. Baxter — Department of Chemical and Biological Engineering, Drexel University, Philadelphia, Pennsylvania 19104, United States; orcid.org/0000-0001-8702-3915; Email: jbaxter@drexel.edu

### **Authors**

Mohammad M. Taheri – Department of Chemical and Biological Engineering, Drexel University, Philadelphia, Pennsylvania 19104, United States; orcid.org/0000-0001-9121-0078

Katherine C. Elbert – Department of Chemistry, University of Pennsylvania, Philadelphia, Pennsylvania 19104, United States

Shengsong Yang — Department of Chemistry, University of Pennsylvania, Philadelphia, Pennsylvania 19104, United States

Benjamin T. Diroll — Center for Nanoscale Materials, Argonne National Laboratory, Lemont, Illinois 60439, United States; © orcid.org/0000-0003-3488-0213

Jungmi Park – Department of Chemistry, University of Pennsylvania, Philadelphia, Pennsylvania 19104, United States

Complete contact information is available at: https://pubs.acs.org/10.1021/acs.jpcc.0c07037

#### **Notes**

The authors declare no competing financial interest.

### ACKNOWLEDGMENTS

The authors acknowledge support from the collaborative NSF grant CHE-1708991 (Drexel) /CHE-1709827 (Penn). K.C.E. acknowledges the support from the NSF Graduate Research Fellowship Program under Grant No. DGE-1321851. C.B.M. acknowledges the Richard Perry University Professorship at the University of Pennsylvania. The use of the Center for Nanoscale Materials, an Office of Science user facility, was supported by the U.S. Department of Energy, Office of Science, Office of Basic Energy Sciences, under Contract No. DE-AC02-06CH11357.

# REFERENCES

- (1) Kamat, P. V. Quantum Dot Solar Cells. Semiconductor Nanocrystals as Light Harvesters. *J. Phys. Chem. C* **2008**, *112*, 18737–18753.
- (2) Robel, I.; Subramanian, V.; Kuno, M.; Kamat, P. V. Quantum Dot Solar Cells. Harvesting Light Energy with CdSe Nanocrystals Molecularly Linked to Mesoscopic TiO2 Films. *J. Am. Chem. Soc.* **2006**, *128*, 2385–2393.
- (3) Hikmet, R. A. M.; Chin, P. T. K.; Talapin, D. V.; Weller, H. Polarized-Light-Emitting Quantum-Rod Diodes. *Adv. Mater.* **2005**, *17*, 1436–1439.
- (4) Shirasaki, Y.; Supran, G. J.; Bawendi, M. G. Bulović, Emergence of colloidal quantum-dot light-emitting technologies. *Nat. Photonics* **2013**, *7*, 933.
- (5) Pal, B. N.; Robel, I.; Mohite, A.; Laocharoensuk, R.; Werder, D. J.; Klimov, V. I. High-Sensitivity p-n Junction Photodiodes Based on Pbs Nanocrystal Quantum Dots. *Adv. Funct. Mater.* **2012**, 22, 1741–1748
- (6) Konstantatos, G.; Howard, I.; Fischer, A.; Hoogland, S.; Clifford, J.; Klem, E.; Levina, L.; Sargent, E. H. Ultrasensitive Solution-Cast Quantum Dot Photodetectors. *Nature* **2006**, 442, 180–183.
- (7) Huang, J.; Mulfort, K. L.; Du, P.; Chen, L. X. Photodriven Charge Separation Dynamics in CdSe/ZnS Core/Shell Quantum Dot/Cobaloxime Hybrid for Efficient Hydrogen Production. *J. Am. Chem. Soc.* **2012**, *134*, 16472–16475.
- (8) Wu, K.; Lian, T. Quantum Confined Colloidal Nanorod Heterostructures for Solar-to-Fuel Conversion. *Chem. Soc. Rev.* **2016**, 45, 3781–3810.
- (9) Chung, D. S.; Lee, J. S.; Huang, J.; Nag, A.; Ithurria, S.; Talapin, D. V. Low Voltage, Hysteresis Free, and High Mobility Transistors from All-Inorganic Colloidal Nanocrystals. *Nano Lett.* **2012**, *12*, 1813–1820.
- (10) Koh, W. K.; Saudari, S. R.; Fafarman, A. T.; Kagan, C. R.; Murray, C. B. Thiocyanate-Capped PbS Nanocubes: Ambipolar Transport Enables Quantum Dot Based Circuits on a Flexible Substrate. *Nano Lett.* **2011**, *11*, 4764–4767.
- (11) Huang, Z.; Tang, M. L. Designing Transmitter Ligands That Mediate Energy Transfer between Semiconductor Nanocrystals and Molecules. *J. Am. Chem. Soc.* **2017**, *139*, 9412–9418.
- (12) De Roo, J.; Huang, Z.; Schuster, N. J.; Hamachi, L. S.; Congreve, D. N.; Xu, Z.; Xia, P.; Fishman, D. A.; Lian, T.; Owen, J. S.; et al. Anthracene Diphosphate Ligands for CdSe Quantum Dots; Molecular Design for Efficient Upconversion. *Chem. Mater.* **2020**, *32*, 1461–1466.
- (13) Alivisatos, A. P. Semiconductor Clusters, Nanocrystals, and Quantum Dots. *Science* **1996**, *271*, 933–937.
- (14) El-Sayed, M. A. Small Is Different: Shape-, Size-, and Composition-Dependent Properties of Some Colloidal Semiconductor Nanocrystals. *Acc. Chem. Res.* **2004**, *37*, 326–333.
- (15) Zhu, H.; Song, N.; Lian, T. Controlling Charge Separation and Recombination Rates in CdSe/ZnS Type I Core-Shell Quantum

- Dots by Shell Thicknesses. J. Am. Chem. Soc. 2010, 132, 15038–15045.
- (16) Maity, P.; Ghorai, N.; Dana, J.; Ghosh, H. N. Impact of One Step Alloying on the Carrier Relaxation and Charge Separation Dynamics of CdxZn1-XSe Graded Nanocrystals. *J. Photochem. Photobiol.*, A 2020, 388, 112131.
- (17) Maity, P.; Ghosh, H. N. Strategies for Extending Charge Separation in Colloidal Nanostructured Quantum Dot Materials. *Phys. Chem. Chem. Phys.* **2019**, *21*, 23283–23300.
- (18) Ghosh, H. N.; Rawalekar, S.; Kaniyankandy, S.; Verma, S. Ultrafast Charge Carrier Relaxation and Charge Transfer Dynamics of CdTe/CdS Core-Shell Quantum Dots as Studied by Femtosecond Transient Absorption Spectroscopy. *J. Phys. Chem. C* **2010**, *114*, 1460–1466.
- (19) Maity, P.; Debnath, T.; Ghosh, H. N. Ultrafast Charge Carrier Delocalization in CdSe/CdS Quasi-Type II and CdS/CdSe Inverted Type i Core-Shell: A Structural Analysis through Carrier-Quenching Study. *J. Phys. Chem. C* **2015**, *119*, 26202–26211.
- (20) Zhao, F.; Li, Q.; Han, K.; Lian, T. Mechanism of Efficient Viologen Radical Generation by Ultrafast Electron Transfer from CdS Quantum Dots. *J. Phys. Chem. C* **2018**, *122*, 17136–17142.
- (21) Zhu, H.; Yang, Y.; Wu, K.; Lian, T. Charge Transfer Dynamics from Photoexcited Semiconductor Quantum Dots. *Annu. Rev. Phys. Chem.* **2016**, 67, 259–281.
- (22) Sharma, S. N.; Pillai, Z. S.; Kamat, P. V. Photoinduced Charge Transfer between CdSe Quantum Dots and P-Phenylenediamine. *J. Phys. Chem. B* **2003**, *107*, 10088–10093.
- (23) Zhu, H.; Yang, Y.; Hyeon-Deuk, K.; Califano, M.; Song, N.; Wang, Y.; Zhang, W.; Prezhdo, O. V.; Lian, T. Auger-Assisted Electron Transfer from Photoexcited Semiconductor Quantum Dots. *Nano Lett.* **2014**, *14*, 1263–1269.
- (24) Wang, H.; McNellis, E. R.; Kinge, S.; Bonn, M.; Cánovas, E. Tuning Electron Transfer Rates through Molecular Bridges in Quantum Dot Sensitized Oxides. *Nano Lett.* **2013**, *13*, 5311–5315.
- (25) Maity, P.; Debnath, T.; Banerjee, T.; Das, A.; Ghosh, H. N. Charge Delocalization in the Cascade Band Structure Cds/Cdse and Cds/Cdte Core-Shell Sensitized with Re(i)-Polypyridyl Complex. J. Phys. Chem. C 2016, 120, 10051–10061.
- (26) Wu, Y.; Li, S.; Gogotsi, N.; Zhao, T.; Fleury, B.; Kagan, C. R.; Murray, C. B.; Baxter, J. B. Directional Carrier Transfer in Strongly Coupled Binary Nanocrystal Superlattice Films Formed by Assembly and in Situ Ligand Exchange at a Liquid-Air Interface. *J. Phys. Chem. C* 2017, 121, 4146–4157.
- (27) Berera, R.; van Grondelle, R.; Kennis, J. T. M. Ultrafast Transient Absorption Spectroscopy: Principles and Application to Photosynthetic Systems. *Photosynth. Res.* **2009**, *101*, 105–118.
- (28) Klimov, V. I. Optical Nonlinearities and Ultrafast Carrier Dynamics in Semiconductor Nanocrystals. *J. Phys. Chem. B* **2002**, *104*, 6112–6123.
- (29) Klimov, V. I.; Mikhailovsky, A. A.; McBranch, D. W.; Leatherdale, C. A.; Bawendi, M. G. Mechanisms for Intraband Energy Relaxation in Semiconductor Quantum Dots: The Role of Electron-Hole Interactions. *Phys. Rev. B-Condens. Matter Mater. Phys.* **2000**, *61*, R13349—R13352.
- (30) Klimov, V.; Bolivar, P. H.; Kurz, H. Ultrafast Carrier Dynamics in Semiconductor Quantum Dots. *Phys. Rev. B-Condens. Matter Mater. Phys.* **1996**, *53*, 1463–1467.
- (31) Pandey, A.; Guyot-Sionnest, P. Slow Electron Cooling in Colloidal Quantum Dots. *Science* **2008**, 322, 929–932.
- (32) Guyot-Sionnest, P.; Wehrenberg, B.; Yu, D. Intraband Relaxation in CdSe Nanocrystals and the Strong Influence of the Surface Ligands. *J. Chem. Phys.* **2005**, 123, No. 074709.
- (33) Cooney, R. R.; Sewall, S. L.; Anderson, K. E. H.; Dias, E. A.; Kambhampati, P. Breaking the Phonon Bottleneck for Holes in Semiconductor Quantum Dots. *Phys. Rev. Lett.* **2007**, *98*, 1–4.
- (34) Sewall, S. L.; Cooney, R. R.; Anderson, K. E. H.; Dias, E. A.; Sagar, D. M.; Kambhampati, P. State-Resolved Studies of Biexcitons and Surface Trapping Dynamics in Semiconductor Quantum Dots. *J. Chem. Phys.* **2008**, *129*, 84701.

- (35) Kambhampati, P. Unraveling the Structure and Dynamics of Excitons in Semiconductor Quantum Dots. *Acc. Chem. Res.* **2011**, *44*, 1–13.
- (36) Efros, A. L.; Rosen, M.; Kuno, M.; Nirmal, M.; Norris, D.; Bawendi, M. Band-Edge Exciton in Quantum Dots of Semiconductors with a Degenerate Valence Band: Dark and Bright Exciton States. *Phys. Rev. B-Condens. Matter Mater. Phys.* **1996**, *54*, 4843–4856.
- (37) Leatherdale, C. A.; Bawendi, M. G. Electron and Hole Relaxation Pathways in Semiconductor Quantum Dots. *Phys. Rev. B-Condens. Matter Mater. Phys.* **1999**, *60*, 13740–13749.
- (38) Sewall, S. L.; Cooney, R. R.; Kambhampati, P. Experimental Tests of Effective Mass and Atomistic Approaches to Quantum Dot Electronic Structure: Ordering of Electronic States. *Appl. Phys. Lett.* **2009**, *94*, 243116.
- (39) Grimaldi, G.; Geuchies, J. J.; Van Der Stam, W.; Du Fossé, I.; Brynjarsson, B.; Kirkwood, N.; Kinge, S.; Siebbeles, L. D. A.; Houtepen, A. J. Spectroscopic Evidence for the Contribution of Holes to the Bleach of Cd-Chalcogenide Quantum Dots. *Nano Lett.* **2019**, 19, 3002–3010.
- (40) Morgan, D. P.; Kelley, D. F. What Does the Transient Absorption Spectrum of CdSe Quantum Dots Measure? *J. Phys. Chem. C* **2020**, *124*, 8448–8455.
- (41) Morgan, D. P.; Maddux, C. J. A.; Kelley, D. F. Transient Absorption Spectroscopy of CdSe Nanoplatelets. *J. Phys. Chem. C* **2018**, 122, 23772–23779.
- (42) Cassette, E.; Pedetti, S.; Mahler, B.; Ithurria, S.; Dubertret, B.; Scholes, G. D. Ultrafast Exciton Dynamics in 2D In-Plane Hetero-Nanostructures: Delocalization and Charge Transfer. *Phys. Chem. Chem. Phys.* **2017**, *19*, 8373–8379.
- (43) Kunneman, L. T.; Schins, J. M.; Pedetti, S.; Heuclin, H.; Grozema, F. C.; Houtepen, A. J.; Dubertret, B.; Siebbeles, L. D. A. Nature and Decay Pathways of Photoexcited States in CdSe and CdSe/CdS Nanoplatelets. *Nano Lett.* **2014**, *14*, 7039–7045.
- (44) Li, Q.; He, S.; Lian, T. How Exciton and Single Carriers Block the Excitonic Transition in Two-Dimensional Cadmium Chalcogenide Nanoplatelets. *Nano Lett.* **2020**, *20*, *6162*–6169.
- (45) Ithurria, S.; Tessier, M. D.; Mahler, B.; Lobo, R. P. S. M.; Dubertret, B.; Efros, A. L. Colloidal Nanoplatelets with Two-Dimensional Electronic Structure. *Nat. Mater.* **2011**, *10*, 936–941.
- (46) Elbert, K. C.; Taheri, M. M.; Gogotsi, N.; Park, J.; Baxter, J. B.; Murray, C. B. Electron Accepting Naphthalene Bisimide Ligand Architectures for Modulation of  $\pi$ – $\pi$  Stacking in Nanocrystal Hybrid Materials. *Nanoscale Horiz.* **2020**, *5*, 1509–1514.
- (47) Carbone, L.; Nobile, C.; De Giorgi, M.; Della Sala, F.; Morello, G.; Pompa, P.; Hytch, M.; Snoeck, E.; Fiore, A.; Franchini, I. R.; et al. Synthesis and Micrometer-Scale Assembly of Colloidal CdSe/CdS Nanorods Prepared by a Seeded Growth Approach. *Nano Lett.* **2007**, 7, 2942–2950.
- (48) Chen, O.; Zhao, J.; Chauhan, V. P.; Cui, J.; Wong, C.; Harris, D. K.; Wei, H.; Han, H. S.; Fukumura, D.; Jain, R. K.; et al. Compact High-Quality CdSe-CdS Core-Shell Nanocrystals with Narrow Emission Linewidths and Suppressed Blinking. *Nat. Mater.* **2013**, *12*, 445–451.
- (49) Sewall, S. L.; Cooney, R. R.; Anderson, K. E. H.; Dias, E. A.; Kambhampati, P. State-to-State Exciton Dynamics in Semiconductor Quantum Dots. *Phys. Rev. B-Condens. Matter Mater. Phys.* **2006**, *74*, 1–8.
- (50) Olshansky, J. H.; Ding, T. X.; Lee, Y. V.; Leone, S. R.; Alivisatos, A. P. Hole Transfer from Photoexcited Quantum Dots: The Relationship between Driving Force and Rate. *J. Am. Chem. Soc.* **2015**, *137*, 15567–15575.
- (51) Olshansky, J. H.; Balan, A. D.; Ding, T. X.; Fu, X.; Lee, Y. V.; Alivisatos, A. P. Temperature-Dependent Hole Transfer from Photoexcited Quantum Dots to Molecular Species: Evidence for Trap-Mediated Transfer. ACS Nano 2017, 11, 8346–8355.
- (52) Hassan, Y.; Janes, T.; Pensack, R. D.; Rafiq, S.; Brodersen, P. M.; Winnik, M. A.; Song, D.; Scholes, G. D. Direct Synthesis of CdSe Nanocrystals with Electroactive Ligands. *Chem. Mater.* **2016**, 28, 4953–4961.

- (53) Tarafder, K.; Surendranath, Y.; Olshansky, J. H.; Alivisatos, A. P.; Wang, L. W. Hole Transfer Dynamics from a CdSe/CdS Quantum Rod to a Tethered Ferrocene Derivative. *J. Am. Chem. Soc.* **2014**, *136*, 5121–5131.
- (54) Ding, T. X.; Olshansky, J. H.; Leone, S. R.; Alivisatos, A. P. Efficiency of Hole Transfer from Photoexcited Quantum Dots to Covalently Linked Molecular Species. *J. Am. Chem. Soc.* **2015**, *137*, 2021–2029.
- (55) Jasieniak, J.; Califano, M.; Watkins, S. E. Size-Dependent Valence and Conduction Band-Edge Energies of Semiconductor Nanocrystals. *ACS Nano* **2011**, *5*, 5888–5902.
- (56) Norris, D.; Bawendi, M. Measurement and Assignment of the Size-Dependent Optical Spectrum in CdSe Quantum Dots. *Phys. Rev. B-Condens. Matter Mater. Phys.* **1996**, *53*, 16338–16346.
- (57) Klimov, V. I.; Schwarz, C. J.; Mc Branch, D. W.; Leatherdale, C. A.; Bawendi, M. G. Ultrafast Dynamics of Inter- and Intraband Transitions in Semiconductor Nanocrystals: Implications for Quantum-Dot Lasers. *Phys. Rev. B-Condens. Matter Mater. Phys.* 1999, 60, R2177–R2180.
- (58) Zhu, H.; Song, N.; Rodríguez-Córdoba, W.; Lian, T. Wave Function Engineering for Efficient Extraction of up to Nineteen Electrons from One CdSe/CdS Quasi-Type II Quantum Dot. *J. Am. Chem. Soc.* **2012**, *134*, 4250–4257.
- (59) Kong, D.; Jia, Y.; Ren, Y.; Xie, Z.; Wu, K.; Lian, T. Shell-Thickness-Dependent Biexciton Lifetime in Type i and Quasi-Type II CdSe@CdS Core/Shell Quantum Dots. *J. Phys. Chem. C* **2018**, *122*, 14091–14098.
- (60) Underwood, D. F.; Kippeny, T.; Rosenthal, S. J. Ultrafast Carrier Dynamics in CdSe Nanocrystals Determined by Femtosecond Fluorescence Upconversion Spectroscopy. *J. Phys. Chem. B* **2001**, *105*, 436–443.
- (61) Lou, Y.; Chen, X.; Samia, A. C.; Burda, C. Femtosecond Spectroscopic Investigation of the Carrier Lifetimes in Digenite Quantum Dots and Discrimination of the Electron and Hole Dynamics via Ultrafast Interfacial Electron Transfer. *J. Phys. Chem. B* **2003**, *107*, 12431–12437.
- (62) Jasieniak, J.; Mulvaney, P. From Cd-Rich to Se-Rich-The Manipulation of CdSe Nanocrystal Surface Stoichiometry. *J. Am. Chem. Soc.* **2007**, *129*, 2841–2848.
- (63) Burda, C.; Chen, X.; Narayanan, R.; El-Sayed, M. A. Chemistry and Properties of Nanocrystals of Different Shapes. *Chem. Rev.* **2005**, 105, 1025–1102.
- (64) Jones, M.; Lo, S. S.; Scholes, G. D. Quantitative Modeling of the Role of Surface Traps in CdSe/CdS/ZnS Nanocrystal Photoluminescence Decay Dynamics. *Proc. Natl. Acad. Sci. U. S. A.* **2009**, *106*, 3011–3016.
- (65) Veamatahau, A.; Jiang, B.; Seifert, T.; Makuta, S.; Latham, K.; Kanehara, M.; Teranishi, T.; Tachibana, Y. Origin of Surface Trap States in CdS Quantum Dots: Relationship between Size Dependent Photoluminescence and Sulfur Vacancy Trap States. *Phys. Chem. Chem. Phys.* **2015**, *17*, 2850–2858.
- (66) Krasselt, C.; Schuster, J.; von Borczyskowski, C. Photoinduced Hole Trapping in Single Semiconductor Quantum Dots at Specific Sites at Silicon Oxide Interfaces. *Phys. Chem. Chem. Phys.* **2011**, *13*, 17084–17092.
- (67) Abdellah, M.; Karki, K. J.; Lenngren, N.; Zheng, K.; Pascher, T.; Yartsev, A.; Pullerits, T. Ultra Long-Lived Radiative Trap States in CdSe Quantum Dots. *J. Phys. Chem. C* **2014**, *118*, 21682–21686.
- (68) Jain, A.; Voznyy, O.; Korkusinski, M.; Hawrylak, P.; Sargent, E. H. Ultrafast Carrier Trapping in Thick-Shell Colloidal Quantum Dots. *J. Phys. Chem. Lett.* **2017**, *8*, 3179–3184.
- (69) Lian, S.; Christensen, J. A.; Kodaimati, M. S.; Rogers, C. R.; Wasielewski, M. R.; Weiss, E. A. Oxidation of a Molecule by the Biexcitonic State of a CdS Quantum Dot. *J. Phys. Chem. C* **2019**, *123*, 5923–5930.
- (70) Li, Q.; Lian, T. Ultrafast Charge Separation in Two-Dimensional CsPbBr 3 Perovskite Nanoplatelets. *J. Phys. Chem. Lett.* **2019**, *10*, 566–573.

(71) Li, Q.; Zhao, F.; Qu, C.; Shang, Q.; Xu, Z.; Yu, L.; McBride, J. R.; Lian, T. Two-Dimensional Morphology Enhances Light-Driven H 2 Generation Efficiency in CdS Nanoplatelet-Pt Heterostructures. *J. Am. Chem. Soc.* **2018**, *140*, 11726–11734.